Birefringence description of a helical fiber-coil

D. Tentori[a], A. Garcia-Weidner[a,*] and E. Ledezma-Sillas[b]
[a]*Applied Physics Division, Optics Department, CICESE,*
Carretera Ensenada Tijuana 3918, Ensenada, B.C. 22860, Mexico,
[*]*e-mail: agarcia@cicese.mx*
[b]*Metalurgy and Structural Integrity Dept., CIMAV,*
Av. Miguel de Cervantes 120, Comp. Ind. Chih., Chih., Mexico, 31136.

Received 23 October 2015; accepted 23 May 2016

Helical coils are used to produce compact fiber devices with stable polarization properties. We have developed a matrix model for such a fiber, taking into account effects of photoelastically induced anisotropy and geometrical phase, on residual birefringence and diattenuation. We present here the theoretical basis used to construct the model and experimental results that validate it.

Keywords: Fiber optics components; Single-mode fibers; Birefringence.

PACS: 42.81.-i; 42.81.Gs; 42.25.Ja

1. Introduction

The polarization properties of a helical coil include strain-induced birefringence, and a geometrical contribution due to the out-of-plane trajectory described by the light beam traveling along the fiber [1-6]. While the geometrical phase can be easily calculated taking into account the helix geometry [7], there is no agreement on how to model the strain-induced birefringence properties of helical coils [8-19].

Helically wound fibers have been mainly applied for the construction of electric current and magnetic sensors [20-23]. In these cases, it has been argued that in addition to the Faraday signal there is an unwanted linear birefringence contribution associated mainly to fiber bending. To minimize or cancel out this unwanted perturbation several methods have been developed [24-30]. Comparing the models reported in the literature [21-30] we noticed there is no agreement on the birefringence description of a helical coil.

There is a wide application of helical coils in polarimetric fiber devices and additional potential uses with erbium-doped fibers are possible. However, to achieve the required optimization of polarization performance in these fibers, it is necessary to gain a clear understanding of their birefringence. In this work we present a birefringence matrix model based on geometric properties of helices and the resulting effects on topological phase contribution [7], and diattenuation. These stress induced and phase contributions have been described using classical polarization optics, and verified experimentally using erbium-doped fibers. To justify the use of a coil built with an erbium-doped fiber it is important to mention that the linear and circular components of their birefringence and their diattenuation are stronger than those observed for helical coils built with standard fibers [31,32].

2. Theory

2.1. Helix

Helix is the out-of-plane curve described by the hypotenuse of a right angle triangle wound around a right circular cylinder when the wrapped cathetus overlaps with the cylinder base. In a Cartesian coordinate system the helix is described by the following equations

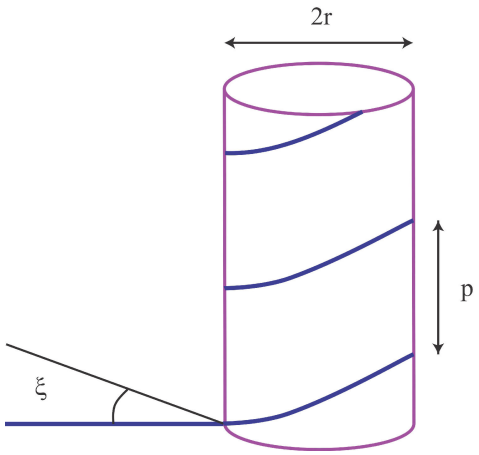

FIGURE 1. Geometrical parameters used to describe a helix: r represents its radius, ξ is the turning angle and p is the pitch.

$$\begin{aligned} x &= r\cos\xi \\ y &= r\sin\xi \\ z &= p\xi/2\pi \end{aligned} \tag{1}$$

where r is the radius of the circular base, ξ is the turning angle shown in Fig. 1 and p is the pitch length of the helix.

The helix curvature describes how fast the tangent vector is changing its direction, and defines the direction of the normal vector along the helix, a unitary vector whose orientation varies along the curve. Curvature κ is given by

$$\kappa = r^2/(r^2+p^2). \tag{2}$$

The vector product of the tangent and normal vectors produces the binormal vector, another unitary vector whose rotation speed at the given point measures the helix torsion τ [33],

$$\tau = p/(r^2+p^2). \tag{3}$$

2.2. Strain-induced birefringence

Practical single-mode fibers are birefringent due to residual stress and the slight deviations of their cross sections from a perfect circular symmetry. The experiments we have performed on standard, erbium-doped [34] and photonic single mode fibers have shown that their residual birefringence corresponds to that of an elliptical retarder (simultaneous combination of linear and circular birefringence). This residual anisotropy is modified by bending and torsion when the fiber is helically wound.

It has been shown that the resulting bend-induced birefringence is linear [35]. Hence, when the helically induced birefringence is the dominant effect, the normal vector associated to this strain defines the orientation of the fast birefringence axis of the fiber.

In regard to torsion, it has been shown that for an optical fiber that behaves as an elliptical retarder, twist-induced birefringence can be described in terms of the product of two matrices. A rotation matrix $\mathbf{R}(b\tau+\beta)$ associated to the gyration of the birefringence axes produced by torsion [36] and a modified elliptical retarder matrix $\mathbf{M}_\tau$ [37]

$$\mathbf{R}(b\tau+\beta)\,\mathbf{M}_\tau\,. \tag{4}$$

In Eq. (4), $\mathbf{M}_\tau$ is the matrix of an elliptical retarder with a retardation angle δ between polarization eigenmodes given by

$$\delta=\delta_0+c\tau\,; \tag{5}$$

where δ_0 is the retardation angle between polarization eigenmodes for the uncoiled (straight) fiber, c is a constant (~ 1) and τ is the applied torsion. As we can see (Eq. 5), the retardation angle between polarization eigenmodes varies linearly with the applied twist. When the twisted fiber is a single-mode erbium-doped fiber, its enhanced induced birefringence allowed noticing that the linear birefringence presents two orthogonal components with an independent twist dependence [38]. Summarizing, in a helical fiber coil, due to the residual elliptical birefringence the fiber has linear and circular birefringence components. In addition, the helical winding contributes with: a) a linear birefringence induced by bending, b) a modification in the linear and circular components of the residual birefringence produced by the applied torsion (Eq. (5)) - this change includes an independent variation of linear birefringence at 0° and linear birefringence at 45° (Jones birefringence), modifying the azimuth ellipticity angles of the coil's elliptical birefringence in reference to the corresponding value for the straight fiber, and c) a geometric rotation. In addition to all these effects, present in every differential segment of the helical coil we must also consider diattenuation. Diattenuation is produced by bending in standard fibers [39] and in laser fibers it is mainly a result of the anisotropic absorption of erbium-doped fibers.

Using the differential matrix calculus developed by R.C. Jones [40] we can deal with the above mentioned simultaneous contributions. Employing this formalism, the differential linear birefringence contributions at 0° and at 45° can be added to produce the total differential linear birefringence contribution. Furthermore, total differential matrices for linear birefringence, circular birefringence and the gyration component are also added to build the total differential retardation matrix.

Twist-induced birefringence in erbium-doped fibers was a case, already solved, which included these contributions [38]. It was shown that the resultant description is equal to the product of a gyration matrix by an elliptical retarder matrix

$$\mathbf{R}(\varsigma)\mathbf{M}_e \tag{6}$$

where the gyration angle ς is in this case equal to $n2\pi(1-\cos\xi)$, being n equal to the number of helix loops [7]. In this work, $\mathbf{M}_e$ is the birefringence matrix of an elliptic retarder with diattenuation [41]

$$\mathbf{M}_e=\frac{A_\alpha}{\gamma^2}[M1\ M2\ M3\ M4]. \tag{7}$$

The column vectors in Eq. (7) are

$$M1=\begin{bmatrix}\gamma^2\cosh\alpha\\ -\alpha R\cos 2\varepsilon_a+\delta V\cos 2\varepsilon\\ \alpha\delta M\sin 2(\varepsilon_a-\varepsilon)\\ -\alpha R\sin 2\varepsilon_a+\delta V\sin 2\varepsilon\end{bmatrix}=\begin{bmatrix}m11\\ m21\\ m31\\ m41\end{bmatrix}$$

$$M2=\begin{bmatrix}-\alpha R\cos 2\varepsilon_a+\delta V\cos 2\varepsilon\\ \frac{1}{2}[\cos\delta(\gamma^2-\alpha^2\cos 4\varepsilon_a-\delta^2\cos 4\varepsilon)+\\ \cosh\alpha(\gamma^2+\delta^2\cos 4\varepsilon+\alpha^2\cos 4\varepsilon_a)]\\ -\delta R\sin 2\varepsilon-\alpha V\sin 2\varepsilon_a\\ -\frac{1}{2}M(\alpha^2\sin 4\varepsilon_a+\delta^2\sin 4\varepsilon)\end{bmatrix}$$

$$=\begin{bmatrix}m12\\ m22\\ m32\\ m42\end{bmatrix}$$

$$M3=\begin{bmatrix}-\alpha\delta M\sin 2(\varepsilon_a-\varepsilon)\\ \delta R\sin 2\varepsilon+\alpha V\sin 2\varepsilon_a\\ \gamma^2\cos\delta\\ -\delta R\cos 2\varepsilon-\alpha V\cos 2\varepsilon_a\end{bmatrix}=\begin{bmatrix}m13\\ m23\\ m33\\ m43\end{bmatrix}$$

$$M4=\begin{bmatrix}-\alpha R\sin 2\varepsilon_a+\delta V\sin 2\varepsilon\\ -\frac{1}{2}M(\alpha^2\sin 4\varepsilon_a+\delta^2\sin 4\varepsilon)\\ \delta R\cos 2\varepsilon+\alpha V\cos 2\varepsilon_a\\ \frac{1}{2}[\cos\delta(\gamma^2-\alpha^2\cos 4\varepsilon_a-\delta^2\cos 4\varepsilon)+\\ \cosh\alpha(\gamma^2+\delta^2\cos 4\varepsilon+\alpha^2\cos 4\varepsilon_a)]\end{bmatrix}$$

$$=\begin{bmatrix}m14\\ m24\\ m34\\ m44\end{bmatrix}$$

where the retardation angle between the elliptical eigenmodes is δ, ε is the birefringence ellipticity angle (Fig. 2a), α is the elliptical absorption, $A_\alpha=e^{-\alpha_o L}$, L is the fiber's length, α_o is the isotropic absorption, ε_α is the angle formed

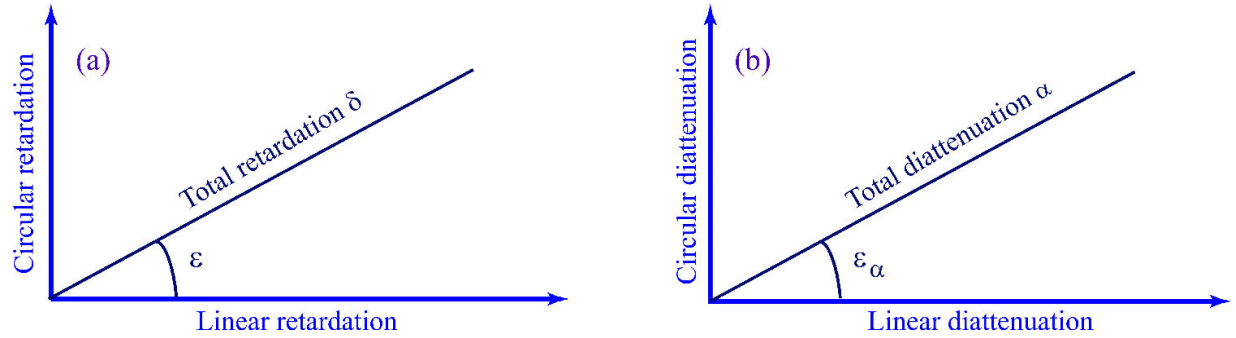

FIGURE 2. The linear and circular birefringence add geometrically. To describe the total retardation the ellipticity angle ε must be specified. Linear and circular diattenuation also add geometrically. The angle between the total diattenuation and its linear component is ε_a.

by the total absorption and the linear component of absorption (Fig. 2b), $\gamma^2 = \delta^2 + \alpha^2$, $R = \delta \sin\delta + \alpha \sinh\alpha$, $V = \alpha \sin\delta - \delta \sinh\alpha$, $M = \cos\delta - \cosh\alpha$ [41]. Up to this point we are assuming that the birefringence axes are aligned with the laboratory reference frame; *i.e.* the azimuth angle of the birefringence matrix is zero.

2.3. Output polarization state

In this work we use linearly polarized input signals with azimuth angle φ, and we assume that the azimuth angle of the fast birefringence axis of the helical coil is θ. For these signals, the output state of polarization (SOP) is given by

$$\mathbf{S}_{\text{out}} = \mathbf{R}(-\theta) \cdot \mathbf{R}(\zeta) \cdot \mathbf{M}_e \cdot \mathbf{R}(\theta) \cdot (1, \cos 2\varphi, \sin 2\varphi, 0)^t \quad (8)$$

where t indicates transpose. Using Eq. 7, the Stokes parameters of the output SOP are:

$$S_0 = \frac{A_\alpha}{\gamma^2}[m_{11} + m_{12}\cos 2(\theta-\varphi) - m_{13}\sin 2(\theta-\varphi)] \quad (9)$$

$$\begin{aligned} S_1 = \frac{A_\alpha}{\gamma^2}\{&\cos 2(\zeta-\theta)[m_{21} + m_{22}\cos 2(\varphi-\theta) \\ &+ m_{23}\sin 2(\varphi-\theta)] + \sin 2(\zeta-\theta)[m_{31} \\ &+ m_{32}\cos 2(\varphi-\theta) + m_{33}\sin 2(\varphi-\theta)]\} \end{aligned} \quad (10)$$

$$\begin{aligned} S_2 = \frac{A_\alpha}{\gamma^2}\{&\cos 2(\zeta-\theta)[m_{31} + m_{32}\cos 2(\varphi-\theta) \\ &+ m_{33}\sin 2(\varphi-\theta)] - \sin 2(\zeta-\theta)[m_{21} \\ &+ m_{22}\cos 2(\varphi-\theta) + m_{23}\sin 2(\varphi-\theta)]\} \end{aligned} \quad (11)$$

$$\begin{aligned} S_3 = \frac{A_\alpha}{\gamma^2}&[m_{41} + m_{42}\cos 2(\theta-\varphi) \\ &- m_{43}\sin 2(\theta-\varphi)] \end{aligned} \quad (12)$$

3. Experiment

The evaluation of the output state of polarization was performed using the semi-automatic polarimetric device shown in Fig. 3. The monochromatic signal from a tunable laser source (TLS, Hewlett Packard 8168C) was circularly polarized by means of a polarization controller. An isolator was used at the TLS output to avoid instabilities produced by reflections. The circularly polarized signal was collimated with a fiber/air coupler c1, and used to illuminate the linear polarizer (P), fixed to a motorized rotating mount supported on an automatic translation stage. The collimated light emerging from the polarizer was coupled (air/fiber coupler c2) to the fiber coil sample (coupler c2 was also fixed to a motorized linear translation stage).

The prism polarizer's orientation was scanned using the motorized rotation stage. The emerging linearly polarized signal was collimated (c3), and traveled through air to another device (c4) used to couple the polarized output signal to a tunable Fabry-Perot filter and to the light polarization analyzer (Agilent 8509C).

For each signal wavelength, coupler c2, the fiber coil, and coupler c3 were removed from the polarimeter optical axis and the collimated signal emerging from the prism polarizer

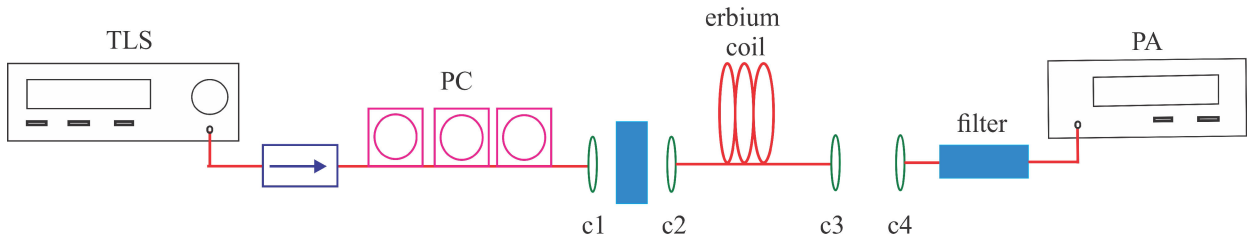

FIGURE 3. Semiautomatic polarimeter. Monochromatic circularly polarized light impinges on the input prism polarizer producing a linearly polarized signal used to illuminate the fiber coil. Light emerging from the helical coil is collimated and inserted in the polarization analyzer.

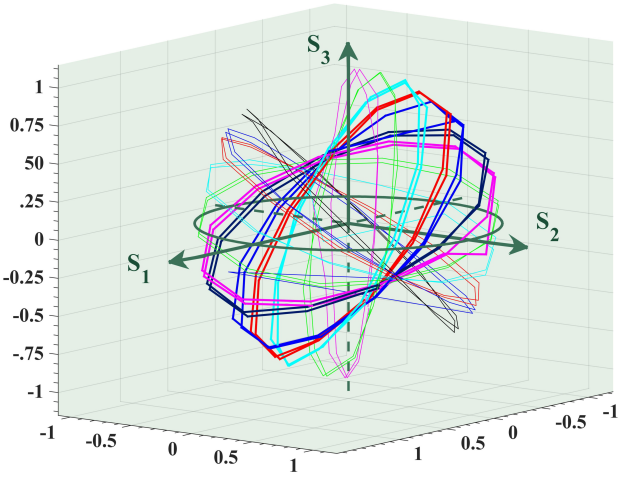

FIGURE 4. Trajectories depicted by the output polarization states. Each color corresponds to a different signal wavelength. Thicker lines were used to highlight the selected wavelengths (magenta-1540, black-1545, blue-1550, red-1555, cyan-1560 nm). Thinner lines correspond to wavelengths between 1517 to 1535 nm and 1565 and 1580 nm.

TABLE I. Erbium fiber used to build the helical coil.

Type	r	pitch	length
402 K5 (INO)	14.8 cm	0.5 cm	8.1 m

the prism polarizer was used to define the polarization analyzer reference frame. To verify the quality of the circular state of polarization emerging from coupler c1, the prism polarizer can also be removed from the set up (afterwards, it can be precisely repositioned using the motorized translation stage).

The evolution of the state of polarization of the signal traveling through the helically wound erbium-doped fiber (Table I) was evaluated using the wavelength scanning technique [34]; *i.e.*, the wavelength of the linearly polarized input signal was varied and the results obtained for the different

wavelengths were compared for a fixed azimuth angle. When using this method, it is assumed that the retardation angle δ between polarization eigenmodes

$$\delta = 2\pi d\Delta n/\lambda \tag{13}$$

presents the same behavior when the fiber length sample d varies (cut back method), as when the wavelength value λ of the light signal is modified. This is true if the fiber birefringence Δn does not change with the signal wavelength.

Here it is necessary to take into account that erbium-doped fibers present an anisotropic absorption; *i.e.*, the value of the birefringence parameter Δn depends on the azimuth angle of the linearly polarized light used to illuminate the sample. Therefore, in order to select a wavelength range in which the variation of the fiber birefringence Δn with wavelength and with the azimuth angle of the input linear polarization could be neglected, we evaluated the variation of the

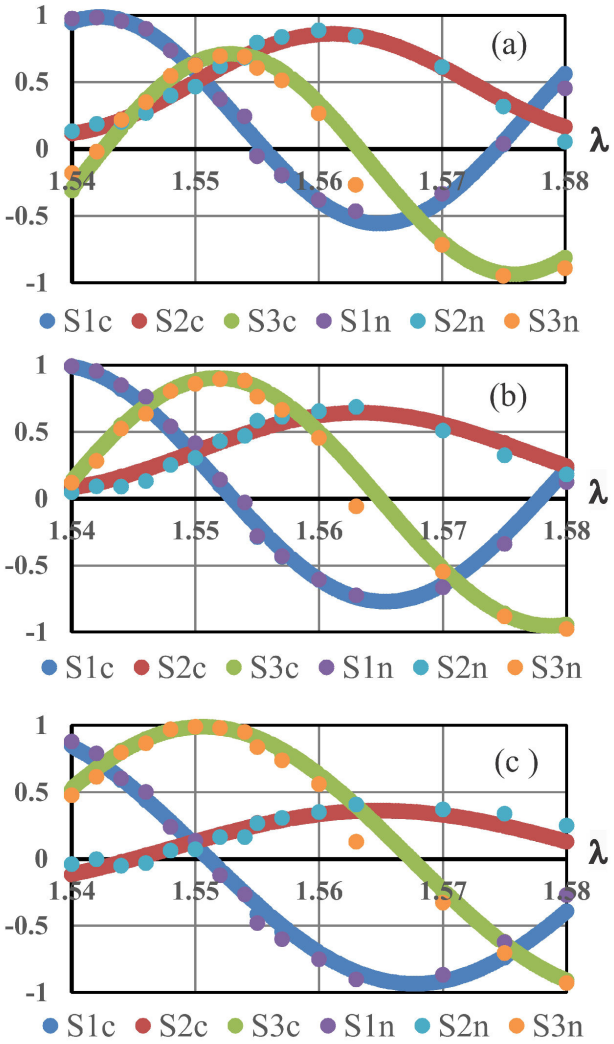

FIGURE 5. Experimental and theoretical values of the Stokes parameters for linearly polarized input signals with azimuth angles equal to a) 10°, b) 20° and c) 30°. Along the horizontal axis we have the signal wavelength in μm.

output state of polarization for a straight sample (1.52 m) of the same fiber used to build the helical coil. The output SOP measured for monochromatic linearly polarized signal wavelengths (1517 and 1570 nm), was evaluated scanning the input azimuth angle from 0 to 360°.

To compare the output states of polarization we minimized the contribution of errors due to coupling and wavelength dependent absorption, normalizing each output Stokes vector. Under these conditions, mapping the results obtained for each signal wavelength in the Poincaré sphere, we obtained two major circles. In Fig. 4 we present these results using a different color for each signal wavelength. The selected wavelengths (1540 to 1560 nm band) have been drawn with thicker lines.

If the fiber birefringence Δn had shown no wavelength dependence, these major circles should have overlapped following the same path. From Fig. 4 we can presume that the

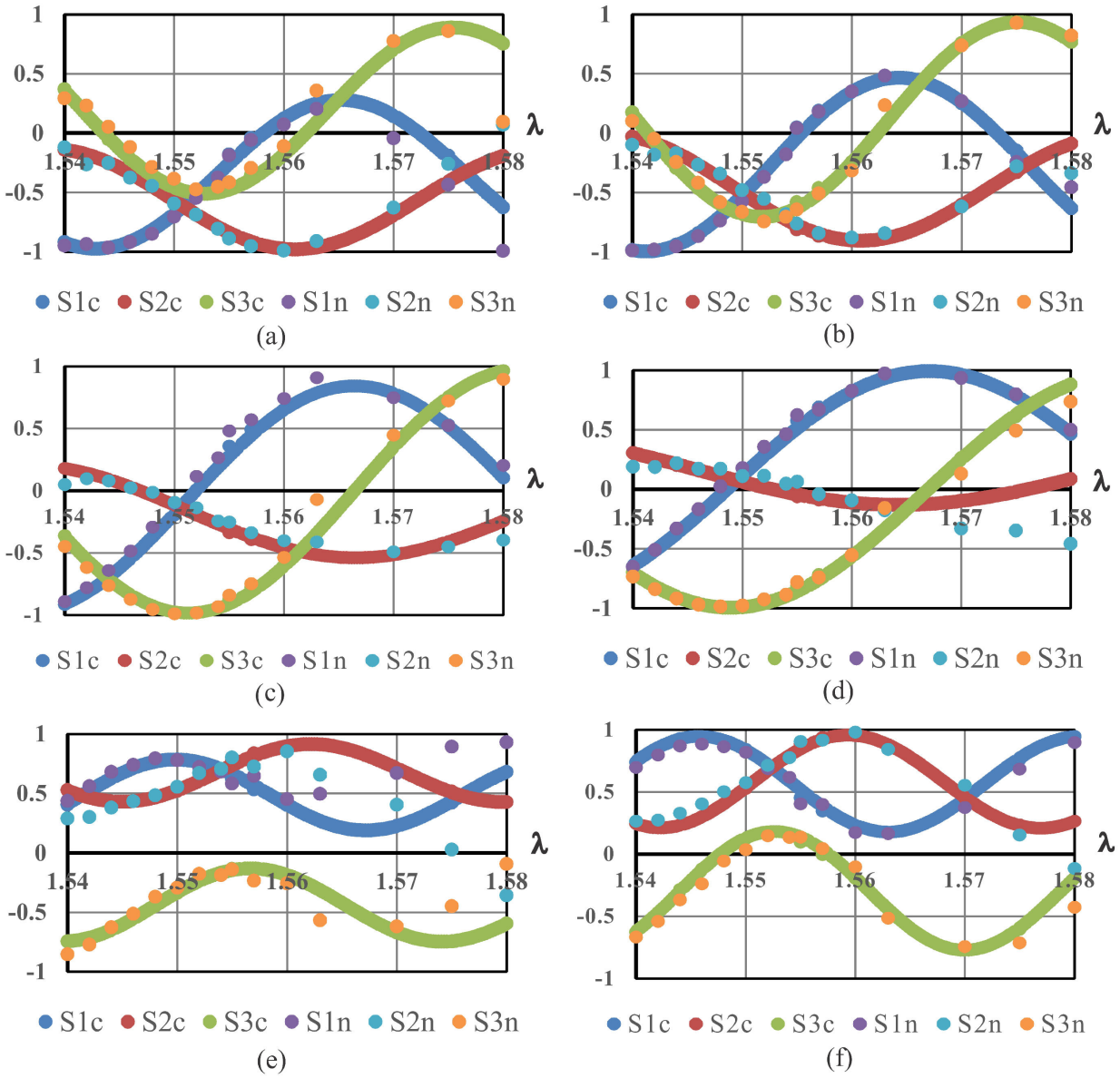

FIGURE 6. Experimental and theoretical values of the Stokes parameters for linearly polarized input signals with azimuth angles equal to a) 90°, b) 100°, c) 120°, d) 130°, e) 160° and f) 170°. Along the horizontal axis we have the signal wavelength in μm. These data present a good fitting from 1.54 to 1.56 μm.

relative similarity is high for those points where these trajectories overlap, and presents stronger variations for those azimuth angles of the input linear state of polarization where these circles move apart.

In regard to the polarization evaluation of the helical coil, the Stokes parameters of the output signal were measured for a fixed wavelength, varying the azimuth angle of the input linear state of polarization from 0 to 180° using a 10° increment. Finally, a different signal wavelength was coupled to the fiber coil. For each wavelength a new calibration of the polarization analyzer was required. We worked with 23 wavelengths from 1500 to 1600 nm. In the following section we discuss the results obtained for signals between 1540 to 1560 nm (selected wavelength range), using additional information measured for a broader wavelength range (1540 to 1580 nm).

4. Analysis of experimental data

In this section we compare the evolution of the state of polarization of the light signal along the fiber, predicted by the theoretical model (Eqs. 10 to 12) with the experimental results measured using the wavelength scanning technique described in Sec. 3. The theoretical values calculated for the Stokes parameters were labeled as S1c, S2c and S3c, and the experimental normalized values as S1n, S2n and S3n.

To perform the comparison minimizing the contribution of errors due to coupling and wavelength dependent absorp-

tion, we normalized each measured output Stokes vector. Accordingly, we also normalized the Stokes vectors calculated using the theoretical model here presented. It is important to notice that normalization preserves the relative magnitude of the Stokes parameters.

We know that as the circular birefringence contribution becomes higher the ellipticity angle ε becomes higher, and when the linear contribution is higher ε becomes lower. Angle ε_α should also present a similar behavior to the variation of the linear and circular components of diattenuation. Figure 5(a) shows that the change of the ellipticity angle was observed ($\varepsilon = 6^\circ$; while in 5(b) and 5(c), $\varepsilon = 2^\circ$), and the influence of the diattenuation angle ε_α could not be detected. This poor sensitivity to the value of ε_α can be explained by the fact that in our model this parameter appears as the argument of a trigonometric function always multiplied by the attenuation coefficient (see the relations after Eq. 7).

Mainly as a result of the change in the ellipticity angle, the frequency of the curves shown in Figs. 5 and 6 varied with the azimuth angle of the linearly polarized input signals.

Regarding linear input polarization states with a 10°, 20° and 30° azimuth angle, the theoretical predictions calculated using the model here presented were confirmed from 1540 to 1580 nm, as we can see in Fig. 5. Likewise, predicted results were confirmed from 1540 to 1560 nm (selected wavelength band) for the input azimuth angles: 90, 100, 120, 130, 160 and 170°, as we can see in Fig. 6. In regard with the ellipticity angle, we can mention that for the curves in Fig. 5, the signals with a smaller azimuth angle ($\varphi = 10^\circ$) were fitted using a larger ellipticity angle (~ 3 times larger than that calculated for $\varphi = 20^\circ$ or 30°). The effect of this additional circular birefringence was associated with the faster variation of the retardation angle α between polarization modes (for $\varphi = 10$ and 30° the absorption coefficient used in the numerical simulation was the same).

An interesting case was the set of curves measured for $\varphi = 120^\circ$, for which the ellipticity angle was equal to zero, indicating that in this case the fiber anisotropy was linear.

In general, for each set of parameters associated with different input azimuth angles (Eqs.10-12) it was necessary to use different values for the retardation (δ) and absorption (α). An effect we associate with the anisotropy of the cross sections of erbium ions in glass [42].

Despite the fact that our data, obtained using the wavelength scanning method limited us to the use of arbitrary units in our analysis, the relative change of the parameters and their relative values allowed to verify the validity of the model here presented for the description of the birefringence of a helically wound single-mode fiber.

5. Conclusion

Using classical polarization optics, a birefringence matrix model for the description of a helically wound optical fiber was presented. This model includes the birefringence induced by the helical winding; *i.e.*, bend induced and twist induced birefringence, the topological rotation of the reference frame and the diattenuation introduced by bending. To include in our model the residual fiber birefringence, the general case of a homogeneous retarder (elliptical birefringence) was assumed. Experimental data obtained for a fiber coil built with a medium absorption erbium-doped fiber show total agreement with the proposed model.

Acknowledgments

We would like to thank Miguel Farfán Sánchez for his help with data collection.

i. Funding Information: CONACYT, project SEP-CONACYT-CB-2010-155121.

1. J.N. Ross, *Opt. Quant. Electron.* **16** (1984) 455-461.
2. F.D.M. Haldane, *Optics letters* **11** (1986) 730-732.
3. E.M. Frins and W. Dultz, *Optics communications* **136** (1997) 354-356.
4. F. Wassmann and A. Ankiewicz, *Applied optics* **37** (1998) 3902-3911.
5. J.Q. Shen and L.H. Ma, *Physics Letters A* **308** (2003) 355-363.
6. G.B. Malykin and V.I. Pozdnyakova, *Physics-Uspekhi* **47** (2004) 289-308.
7. D. Tentori, C. Ayala-Díaz, F. Treviño-Martínez, F.J. Mendieta-Jiménez and H. Soto-Ortiz, *Journal of Modern Optics* **48** (2001) 1767-1780.
8. A. Papp and H. Harms, *Applied optics* **16** (1977) 1315-1319.
9. S.C. Rashleigh and R. Ulrich, *Optics letters* **5** (1980) 354-356.
10. N. Shibata, M. Tsubokawa, M. Ohashi, K. Kitayama and S. Seikai, *J. Opt. Soc. Am. A* **3** (1986) 1935-1940.
11. C. Tsao, *J. Opt. Soc. Am. A* **4** (1987) 1407-1412.
12. T. Eftimov and T. Kortenski, *J. Mod. Optics* **36** (1989) 287-304 .
13. M.W. Shute, C.S. Brown and J. Jarzynski, *J. Opt. Soc. Am. A* **14** (1989) 3251-3261.
14. V. Krylov and L.I. Slepyan, *Physical Review B* **55** (1977) 14067-14070.
15. M. Sumetsky, *Optics Express* **12** (2004) 2303-2316.
16. Z. Menachem and M. Mond, *Progress In Electromagnetics Research* **61** (2006) 159-192.
17. N.J. Muga, A.N. Pinto, M.F. Ferreira and J.R. Ferreira da Rocha, *J. Lightwave Technol.* **24** (2006) 3932-3943.
18. C.N. Alexeyev and M.A. Yavorsky, *Journal of Optics A: Pure and Applied Optics* **8** (2006) 647-651.

19. S.K. Morshnev *et al*., *Quantum Electronics* **39** (2009) 287-292.

20. A.M. Smith, *Applied Optics* **17** (1978) 52-56.

21. S.C. Rashleigh and R. Ulrich, *Applied Physics Letters* **34** (1979) 768-770.

22. G. Day, D. Payne, A. Barlow and J. Ramskov-Hansen, *Opt. Lett.* **7** (1982) 238-240.

23. F. Maystre and A. Bertholds, *Optics letters* **14** (1989) 587-589.

24. M. Grexa, G. Hermann, G. Lasnitschka and A. Scharmann, *Applied Physics B* **35** (1984)145-148.

25. Z.B. Ren and P. Robert, *Optics letters* **14** (1989) 1228-1230.

26. D. Tang, A.H. Rose, G.W. Day and S. M. Etzel, *J. Lightwave Technol*. **9** (1991) 1031-1037.

27. S.X. Short, J.U. de Arruda, A.A. Tselikov and J.N. Blake, *J. Lightwave Technol.* **16** (1998) 1844-1850.

28. C.D. Perciante and J.A. Ferrari, *Applied optics* **45** (2006) 1951-1956.

29. C. Zhang, C. Li, X. Wang, L. Li, J. Yu and X. Feng, *Applied optics* **51** (2012) 3977-3988.

30. S. Xu, W. Li, Y. Wang and F. Xing, *Applied optics* **53** (2014) 5486-5492.

31. A. Eyal, N. Friedman and M. Tur, 10th Meeting on Optical Engineering in Israel, *International Society for Optics and Photonics* (1997) 415-422.

32. D. Tentori, *et al*. *2001 Spectral birefringence characterization of helically wound monomode erbium-doped fibers ITCom 2001: International Symposium on the Convergence of IT and Communications, International Society for Optics and Photonics* (2001) 467-476.

33. C.H. Tang, Microwave Theory and Techniques, *IEEE Transactions on* **18** (1970) 69-69.

34. F. Treviño-Martínez, D. Tentori, C. Ayala-Díaz and F. Mendieta-Jiménez, *Optics express* **13** (2005) 2556-2563.

35. R. Ulrich, S.C. Rashleigh and W. Eickhoff, *Optics letters* **5** (1980) 273-275.

36. D. Tentori, C. Ayala-Díaz, E. Ledezma-Sillas, F. Treviño-Martínez and A. García-Weidner, *Optics communications* **282** (2009) 830-834 .

37. D. Tentori, A. García-Weidner and C. Ayala-Díaz, *Optical Fiber Technology* **18** (2012) 14-20.

38. D. Tentori and A. García-Weidner, *Optics express* **21** (2013) 31725-31739.

39. L. Faustini and G. Martini, *J. Lightwave Technol.* **15** (1997) 671-679.

40. R.C. Jones, *J. Opt. Soc. Am.* **38** (1948) 671-683.

41. A. García-Weidner and D. Tentori, "Mueller matrix for an elliptical birefringent media with dichroism", to be published.

42. S. Ono and S. Tanabe, *IEEE Journal of* **40** (2004) 1704-1708.